Ionization and dissociation energies of HD and dipole-induced g/u-symmetry breaking

N. Hölsch, I. Doran, and F. Merkt[*]
Institute for Molecular Physical Science, ETH Zürich, 8093 Zürich, Switzerland

J. Hussels, C.-F. Cheng,[†] E. J. Salumbides, H. L. Bethlem, K. S. E. Eikema, M. Beyer, and W. Ubachs[‡]
Department of Physics and Astronomy, LaserLaB, Vrije Universiteit Amsterdam, de Boelelaan 1081, 1081 HV Amsterdam, The Netherlands

Ch. Jungen[§]
Université Paris-Saclay, Centre National de la Recherche Scientifique, Laboratoire Aimé Cotton, 91400 Orsay, France

(Received 29 March 2023; accepted 22 June 2023; published 22 August 2023)

The ionization energy of HD has been determined to be $E_I(\mathrm{HD}) = 124\,568.484\,66(7)\,\mathrm{cm}^{-1}$ by two-photon Doppler-free vacuum-ultraviolet pulsed laser spectroscopy, near-infrared continuous-wave laser spectroscopy, and Rydberg-series extrapolation by multichannel quantum-defect theory (MQDT). From this value, the dissociation energy of HD is deduced to be $D_0(\mathrm{HD}) = 36\,405.782\,53(7)\,\mathrm{cm}^{-1}$, representing a fivefold improvement over previous values and resolving a 3.2σ disagreement with *ab initio* calculations of the four-particle nonadiabatic relativistic energy and of quantum-electrodynamic corrections up to order $m\alpha^6$. Interactions between d, f, and g Rydberg series have been observed and had to be included in the MQDT extrapolation of the Rydberg series.

DOI: 10.1103/PhysRevA.108.022811

I. INTRODUCTION

Considerable progress has been made recently in first-principles calculations of the level energies and transition frequencies of two-electron molecules. The most accurate calculations account for nonadiabatic effects in a full, four-particle treatment of the nuclei, i.e., without relying on the Born-Oppenheimer approximation. Relativistic and radiative corrections are determined by perturbation theory up to high orders in the fine-structure constant [1–3]. Intervals between the lowest rovibrational levels of H_2 can be predicted to better than 100 kHz, and even the reported uncertainties in the calculated dissociation energies of H_2, HD, and D_2 are less than 1 MHz [4]. This level of accuracy makes molecular hydrogen an attractive system for frequency metrology, with the prospect of gaining information on nuclear charge radii, obtaining improved values of the proton-to-electron and deuteron-to-electron mass ratios, and potentially even discovering incomplete aspects of the standard model of particle physics [5].

The validation of the underlying theory and computational procedures requires accurate measurements of energy intervals in these molecules (primarily H_2, HD, and D_2). Efforts at measuring intervals between rotational, vibrational, and electronic energy levels in molecular hydrogen are underway in several laboratories [6–15]. Measuring different transitions enables one to obtain energy intervals with specific dependences on the physical constants used as input parameters in the first-principles calculations, and with different relative contributions from nonadiabatic, relativistic, radiative, and finite-nuclear-size effects. Typically, the effects of most contributions tend to partially cancel out in the transition energies, especially in the case of transitions involving small changes of the rotational and vibrational motion, because the quantum states connected by the transitions exhibit very similar nonadiabatic, relativistic, and radiative corrections. In contrast, measurements of dissociation and ionization energies connect the tightly bound ground state of molecular hydrogen to quantum states of very different physical systems, two hydrogen (deuterium) atoms in the case of the dissociation energy and a free electron and a molecular ion in the case of the ionization energy. This connection is very attractive in the case of H_2, HD, and D_2 because the fragments (H, D, H_2^+, HD^+, and D_2^+) are fundamental one-electron systems that are extremely well characterized by experiment [16–20] and theory [21–23]; for details see also the new CODATA18 revision [24].

The present paper reports on a new measurement of the ionization $E_I(\mathrm{HD})$ and dissociation $D_0(\mathrm{HD})$ energies of HD and complements recent measurements of the same quantities in H_2 [12,25,26] and D_2[27]. Unlike earlier work, which relied on the direct determination of the onset of dissociation continua in the spectra of molecular hydrogen [28–30], the

[*]frederic.merkt@phys.chem.ethz.ch
[†]Present address: Department of Chemical Physics, University of Science and Technology of China, Hefei 230026, China.
[‡]w.m.g.ubachs@vu.nl
[§]christian.jungen@universite-paris-saclay.fr

focus lies on the determination of sharp transitions between the ground state and high-lying Rydberg states belonging to series converging on the ground state of the cation. The ionization energy is obtained by extrapolation of the Rydberg series to their limits using multichannel quantum-defect theory (MQDT). This approach was pioneered by Herzberg and Jungen, who used it to determine the ionization energy of H_2 and the rovibrational energy level structure of the $X\,^2\Sigma_g^+$ ground electronic state of H_2^+ at a precision of about 10 GHz from the vacuum-ultraviolet (VUV) absorption spectrum of H_2 already in 1972 [31]. The dissociation energy is then derived from the thermochemical cycle:

$$D_0(\mathrm{HD}) = E_\mathrm{I}(\mathrm{HD}) + E_\mathrm{I}(\mathrm{HD}^+) - E_\mathrm{I}(\mathrm{H}) - E_\mathrm{I}(\mathrm{D}),$$

using the accurate values for the ionization energy of the molecular ion, $E_\mathrm{I}(\mathrm{HD}^+)$, and for the ionization energy of the atoms, $E_\mathrm{I}(\mathrm{H})$ and $E_\mathrm{I}(\mathrm{D})$, which are known with extreme precision, as discussed above.

Our approach consists in determining the energy interval between the ground state of molecular hydrogen and high Rydberg states as the sum of three intervals [32] corresponding to (i) two-photon transitions from the ground state to a selected rovibrational level of a low-lying electronic state, such as the EF and $GK\,^1\Sigma_g^+$ states, measured by Doppler-free two-photon spectroscopy in the Amsterdam laboratory; (ii) single-photon transitions from the selected low-lying level to high Rydberg states measured in the Zurich laboratory; and (iii) the binding energy of the Rydberg states obtained by MQDT using programs developed in Orsay [33]. Although the use of MQDT might appear to make this procedure a mixed experimental-theoretical approach, the quantum-defect parameters, initially obtained in first-principles calculations (see, e.g., Ref. [34]), are extensively refined and validated by comparison with experimental results obtained for different Rydberg series and in different ranges of the principal quantum number (see, e.g., Refs. [35,36]). The detailed excitation scheme and level diagram are analogous to those presented in Fig. 1 of Ref. [27].

In 2009–2010, the ionization energies of H_2 [37], HD [38], and D_2 [39] were measured using supersonic beams generated with pulsed valves operated at room temperature. Pulsed lasers were used and their frequencies were calibrated with transitions of molecular iodine as reference, resulting in an overall accuracy of about 10–15 MHz. The EF state was used as intermediate level. In all three cases, the experimental results agreed within their errors with the theoretical results obtained in Warsaw [40,41].

In the current experimental approach, applied so far to H_2 and D_2, the transition frequencies to the low-lying states are measured by two-photon Doppler-free Ramsey-comb spectroscopy in the case of the X-EF interval [11,42] and by two-photon Doppler-free VUV spectroscopy in the case of the X-GK interval [25,27]. The energy intervals from these low-lying states to high Rydberg states are then determined using single-mode cw laser spectroscopy and all frequencies are stabilized using frequency combs and referenced to a Rb or Cs frequency standard. Cryogenic valves are used to produce supersonic beams of higher densities and lower mean velocities. Instead of measuring p Rydberg series, transitions to nonpenetrating f Rydberg states are used, which are less perturbed than the p series and thus more convenient to use in the Rydberg series extrapolation. For H_2 and D_2, these improvements resulted in a more than tenfold accuracy improvement over the 2009–2010 experiments. A similar improvement in the accuracy of the calculations was achieved in a parallel effort [3,4]. The new results obtained for H_2 and D_2 agree within twice the combined experimental and theoretical uncertainties. However, in the case of HD, the new theoretical results $D_0(\mathrm{HD}) = 36\,405.782\,54(21)\ \mathrm{cm}^{-1}$ in 2018 [43] and $36\,405.782\,477(26)\ \mathrm{cm}^{-1}$ in 2019 [4] increased the discrepancy with the 2009 experimental result to 3.2σ, dominated by the experimental uncertainty.

The primary aim of the investigation presented here is to clarify the situation by remeasuring the dissociation energy of HD with the new approach. The experimental scheme involves stepwise excitation through the GK state, as performed in the recent measurement of the dissociation energy of D_2 [27]. A special feature of HD compared to H_2 and D_2 is the mass asymmetry, which results in the mixing of states of g and u symmetry through the dipole of the HD^+ core arising from the separation of the center of mass from the center of charge [44,45]. The corresponding spectral perturbations, which were found to be on the order of several MHz for the $np1_1$ series interacting with the $nd2_1$ series [46], were found to also affect the $nf0_3$ series and had to be included in the MQDT treatment of the Rydberg-series extrapolation. The characterization of these perturbations represents the second focus of the present investigation.

II. *GK*-STATE SPECTROSCOPY IN AMSTERDAM

In the Amsterdam laboratory, two-photon Doppler-free spectroscopy in the VUV is performed to measure the frequency of the transition between the $X\,^1\Sigma_g^+(v''=0, N''=0)$ ground and the $GK\,^1\Sigma_g^+(v'=1, N'=2)$ excited state of HD, referred to as the $GK(1,2)$-$X(0,0)$ frequency below. The $GK(1,2)$ state was chosen rather than the longer-lived $GK(0,0)$ and $GK(0,2)$ states because of its larger Franck-Condon factor for nonresonant two-photon excitation from the ground state. As in H_2 and D_2, the transition to the $GK(1,0)$ was found to be very weak. Only after long-time averaging could a very weak signal be obtained when probing the $Q(0)$ two-photon transition, at an intensity level two orders of magnitude lower than the $S(0)$ line used in the present investigation. Because such a discrepancy cannot be explained on the basis of Hönl-London factors, we postulate that the two-photon excitation borrows its strength through mixing of the GK final state of $^1\Sigma_g^+$ symmetry with a neighboring state of $^1\Pi_g$ symmetry. This mixing cannot occur for $N'=0$ levels because such levels do not exist in a $^1\Pi_g$ rotational manifold, but occurs for $N'=2$ levels. The experimental procedure and apparatus are the same as those presented in the previous determination of the ionization energy of D_2 [27] and only a short summary of the most relevant aspects is provided here.

The gas sample is a cold, skimmed supersonic beam of a mixture consisting of 25% H_2, 25% D_2, and 50% HD emitted by a liquid-N_2-cooled pulsed valve (nozzle opening diameter of 0.8 mm, valve opening time of 20 µs, repetition rate 10 Hz) developed in Zurich [47], with the reservoir held at a

stagnation pressure of 9 bar. The supersonic beam is crossed at right angles by two counterpropagating tunable VUV laser beams of identical wavelength around 179 nm that are used to induce the $GK(1,2)$-$X(0,0)$ two-photon transition. Ionization from the $GK(1,2)$ state is achieved using a second laser with wave number tunable in the range between 12 600 and 12 700 cm^{-1}. To enhance the ionization yield and improve the signal-to-noise ratios of the two-photon Doppler-free spectra, the frequency of this laser is fixed at the position of a transition from the $GK(1,2)$ intermediate state to a selected autoionizing resonance located just above the first ionization threshold of HD. This measure enables one to considerably reduce the intensity of the second laser and thus minimize undesirable ac Stark shifts of the two-photon transition. Because the lifetime of the $GK(1,2)$ level of HD is comparable to the laser pulse durations (see Sec. III), the two lasers are temporally overlapped for efficient ionization.

The VUV laser radiation, with wavelength tunable around 179 nm, is generated by frequency up-converting the output of a Fourier-transform-limited, seeded Ti:Sa laser system (fundamental wavelength of ≈716 nm) in two subsequent second-harmonic-generation stages, the first consisting of a β-barium-borate and the second of a $KBe_2BO_3F_2$ (KBBF) nonlinear crystal (see Ref. [48] for details). The seed-laser beam is obtained from the single-mode output of a Ti:Sa ring laser with frequency locked to a frequency comb and referenced to a Cs clock, resulting in a frequency stability $(\Delta\nu/\nu)$ of 10^{-12}. The laser frequency is controlled using a double-pass acousto-optic modulator (AOM) and can be scanned over ranges of up to 790 MHz by changing the AOM modulation frequency. Pulse amplification is achieved in a Nd:YAG-laser-pumped Ti:Sa oscillator-amplifier system [49]. Frequency chirp effects and cavity-mode pulling effects in the output of the titanium sapphire (Ti:Sa) oscillator-amplifier laser system were monitored and actively counteracted by placing an electro-optic modulator (EOM) in the oscillator cavity [48]. After chirp compensation by the EOM, the remaining chirp was measured on a shot-to-shot basis and numerically corrected for.

The two-photon Doppler-free spectra were recorded by scanning the VUV laser frequency in steps of 1.6 MHz and monitoring the HD^+ ionization signal after extraction of the HD^+ ions with a pulsed electric field towards a microchannel-plate (MCP) detector connected to a CCD camera in a direction perpendicular to the HD-beam propagation axis. Small Doppler shifts arising from a slight deviation from 180° of the two counterpropagating VUV laser beams were measured by changing the velocity of the supersonic beam through control of the valve temperature.

Figure 1(b) illustrates the procedure followed to determine and compensate the Doppler shifts of the two-photon transition frequency. The procedure involved measuring the two-photon transition frequencies for two different beam velocities (about 1850 and 1000 m/s, obtained with the pulsed valve held at room temperature and 77 K, respectively) on eight different days after full realignment of the two counterpropagating laser beams. The time delays between the triggers for the opening of the pulsed valve and for the laser pulses reaching the interaction region were calibrated and converted

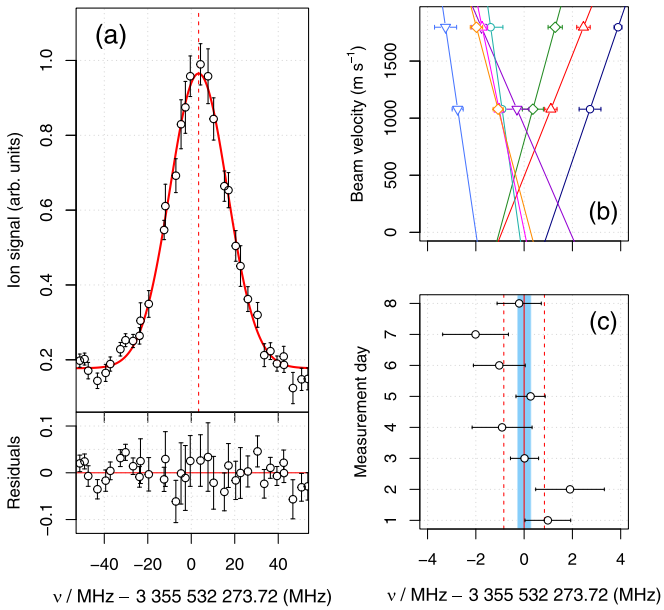

FIG. 1. (a) Comparison of a chirp-compensated spectrum of the $GK\ ^1\Sigma_g^+(1,2) \leftarrow X\ ^1\Sigma_g^+(0,0)$ two-photon transition of HD (open circles) with the fitted Gaussian line profile (full red line) and fit residuals (lower panel). (b) Linear extrapolations to zero beam velocity of the Doppler shifts measured using HD beams of 1850- and 1000-m/s mean velocities. The different colors represent distinct alignments of the counterpropagating VUV beams. (c) Extrapolated Doppler-free transition frequencies. The dashed red lines indicate the standard deviation (0.88 MHz), reflecting the combined uncertainties from the statistical error and errors resulting from imperfect compensations of the first-order Doppler shift and frequency chirps. The solid red line at 3 355 532 273.72 MHz is the average value and the blue area represents the standard error of the mean (0.31 MHz) of the eight measurements.

into values of the velocities of the HD molecules probed spectroscopically, as explained in Sec. 6.3.2 of Ref. [50] (see Fig 6.5). Each new alignment corresponds to a slightly different deviation from an exact counterpropagating arrangement and thus leads to a slightly different linear Doppler shift. The transition frequencies were corrected for the second-order Doppler shifts of about −60 and −20 kHz for the velocities of 1850 and 1000 m/s, respectively, with an overall uncertainty of 30 kHz, leaving only the linear Doppler shift to correct for. The Doppler-free transition frequency was obtained by linearly extrapolating the measured transition frequencies to zero velocity, as indicated by the colored lines, which correspond to distinct laser alignments. The eight Doppler-free frequencies determined in this manner are depicted in Fig. 1(c). They have an average of 3 355 532 273.72 MHz, a standard deviation of 0.88 MHz, and a standard error of the mean of 0.31 MHz, which are limited by the effects of imperfect compensations of the first-order Doppler effect and frequency chirps.

To compensate for ac Stark shifts, the $GK(1,2)$-$X(0,0)$ transition frequency was measured for different pulse energies of the involved lasers and extrapolated to zero pulse energies, following the same procedure as in our previous study of the $GK(1,2)$-$X(0,0)$ transition of D_2 [27]. The details of the

TABLE I. Error budget of the measurement of the $GK\ ^1\Sigma_g^+(1,2) \leftarrow X\ ^1\Sigma_g^+(0,0)$ transition in HD.

Measured frequency		3 355 532 273.72 MHz
Effect	Correction	Uncertainty
Residual first-order Doppler		$(310\ \text{kHz})_{\text{stat}}$
Second-order Doppler	See text	30 kHz
Ac Stark ionization laser	−50 kHz	100 kHz
Ac Stark VUV laser	100 kHz	160 kHz
$GK(1,2)$ hyperfine structure		100 kHz
Final frequency		3 355 532 273.67(38) MHz

analysis for HD can be found in the dissertation of Hussels (see, in particular, Figs. 6.3 and 6.4 of Ref. [50]). The ranges over which the pulse energies were varied are 1 to 2.7 mJ for the blue light used to generate the VUV radiation in the KBBF crystal, and 0.1 to 0.6 mJ for the second (ionization) laser. The ac Stark shifts were at the detection limit and the extrapolated values with their uncertainties are listed in Table I.

Table I presents the error budget of the determination of the $GK(1,2)$-$X(0,0)$ transition frequency. The main source of uncertainty originates from the statistical uncertainty in the analysis of the Doppler shifts and frequency chirps (310 kHz), followed by the uncertainties in the determination of the ac Stark shifts induced by the VUV laser (160 kHz) and the ionization laser (100 kHz). In a two-photon excitation with counterpropagating laser beams, there is no recoil effect and only a residual first-order Doppler shift arising from imperfect alignment of the counterpropagating lasers.

An additional uncertainty contribution was included to account for the fact that the hyperfine structures of the $X(0,0)$ and $G(1,2)$ states were not resolved in the experimental spectra. Measurements of the hyperfine structure of the $X(0,0)$ ground state indicate a splitting of about 50 Hz [51], in agreement with a recent *ab initio* calculation [52]. Calculations of hyperfine effects in the X ground state of HD reveal that for $N'' = 2$ the hyperfine structure spans a few hundred kHz [53]. Similar calculations comparing hyperfine effects in the ground and excited states of $^1\Sigma_g^+$ symmetry in hydrogen show that the span covered by the different components is of similar size, even somewhat smaller in the excited states [54]. Computational modeling of possible shifts of the center of gravity of a rovibrational transition with a hyperfine span of such size in HD for the case of unresolved hyperfine structure by two independent groups has demonstrated that the overall shift resulting from hyperfine effects is well below 100 kHz [55,56]. We adopt a conservative contribution of 100 kHz to the uncertainty imposed by underlying hyperfine structure, yielding a final value of 3 355 532 273.67(38) MHz for the frequency of the $GK(1,2)$-$X(0,0)$ transition.

III. RYDBERG SPECTROSCOPY IN ZURICH

The goal of the experiments carried out in Zurich is to determine the binding energy of the $GK\ ^1\Sigma_g^+(1,2)$ state accessed in Amsterdam, i.e., connect it to the first ionization limit of HD. As in the previous study of D_2 [27], transitions to high-n Rydberg states are measured from the $GK(0,2)$ level and the binding energy of this initial state is determined by extrapolation of the Rydberg series to the ionization threshold. The $GK(0,2)$ level is more advantageous than the $GK(1,2)$ level for high-precision measurements because its lifetime is longer. The lifetimes of the $GK(0,2)$ and $GK(1,2)$ were determined to be 154(4) and 18.7(3) ns, respectively, using the pump-probe scheme described in Ref. [57]. The relative position of the two states was determined by measuring the transition frequencies to the same final Rydberg state, the $(G_1^+ = 0, G^+ = F^+ = 1)$ hyperfine component of the $65f0_3$ Rydberg state (see discussion of the Rydberg-state hyperfine structure, and in particular Fig. 5, below). Systematic errors related to the Stark and Doppler shifts cancel out when building the difference of the two transition frequencies so that the uncertainty reduces to 50 kHz (see Table IV below).

The intermediate GK states are accessed from the $X\ ^1\Sigma_g^+(0,0)$ ground state in a resonant two-photon excitation scheme via the $B\ ^1\Sigma_u^+(4,1)$ state using pulsed laser sources in the VUV (≈105 nm) and visible (≈595 nm) ranges. High-n Rydberg states are then excited from the selected intermediate GK rovibrational level either with pulsed laser radiation for survey spectra or using single-mode continuous-wave near-infrared (NIR) radiation from a Ti:Sa laser (bandwidth of 1 MHz) for high-resolution spectra. The complete resonant three-photon excitation is thus

$$\begin{aligned} X\ ^1\Sigma_g^+(0,0) &\xrightarrow{\text{VUV}} B\ ^1\Sigma_u^+(4,1) \\ &\xrightarrow{\text{VIS}} GK\ ^1\Sigma_g^+(0,2)\,\text{or}\,(1,2) \\ &\xrightarrow{\text{NIR}} npN_N^+/nfN_N^+\ [\text{H}_2^+ X^+(v^+ = 0)], \end{aligned} \quad (1)$$

and is performed in a pulsed skimmed supersonic beam of HD emanating from a cryogenic valve cooled to 60 K (stagnation pressure of 2 bars, repetition rate 25 Hz). Spectra are recorded by monitoring the HD^+ ions produced by pulsed field ionization or autoionization of the Rydberg states. The pulsed electric field used for field ionization also extracts the ions and accelerates them toward an MCP detector. The laser system, apparatus, and measurement procedures are analogous to those used in the study of D_2 and have been described in Ref. [59].

An absolute NIR-frequency accuracy of better than 20 kHz is achieved by stabilizing the narrow-band Ti:Sa laser to a frequency comb which is referenced to a Rb GPS standard. In order to cancel the first-order Doppler shift, a retroreflecting mirror placed beyond the measurement chamber is carefully adjusted to overlap the reflected NIR laser beam with the incoming beam at a distance of ≈10 m from the mirror. Because of a slight deviation from a 90° angle between the laser-propagation and molecular-beam axes, this procedure leads to two Doppler components with equal but opposite shifts. The Doppler-free transition frequency is obtained by averaging the two center frequencies, which cancels the first-order Doppler shift to better than 200 kHz in a single measurement, and correcting for the second-order Doppler and photon-recoil shifts. Averaging over several independent measurements after full realignment of the optical layout transfers the systematic uncertainty from the residual first-order Doppler shift to a contribution to the overall statistical uncertainty, which is

TABLE II. Systematic (syst.) and statistical (stat.) uncertainties for the transition from the $GK(0,2)$ state of HD to the $65f0_3(G_1^+ = 0, G^+ = F^+ = 1)$ Rydberg state resulting from a series of independent measurements. See text for details.

Measured frequency		386 645 211.44 MHz
	Correction	Uncertainty
Dc Stark shift		60 kHz
Ac Stark shift		≈5 kHz
Zeeman shift		≈10 kHz
Pressure shift		≈1 kHz
Second-order Doppler shift	+2 kHz	0.5 kHz
Line-shape model		50 kHz
Photon-recoil shift	−110 kHz	
Syst. uncertainty		125 kHz
Stat. uncertainty, incl. First-order Doppler shift		40 kHz
Final frequency	$386\,645\,211.33(4)_{\mathrm{stat}}(13)_{\mathrm{sys}}$ MHz	

40 kHz. Table II lists the error budget of the determination of the $65f0_3(G_1^+ = 0, G^+ = F^+ = 1) \leftarrow GK(0, 2)$ transition.

Figure 2 shows a low-resolution overview spectrum of Rydberg states excited from the $GK(0,2)$ state using pulsed laser radiation. The colored bars denote the zero-quantum-defect positions of Rydberg series converging to the $N^+ = 0$ (blue), $N^+ = 1$ (orange), and $N^+ = 2$ (pink) rotational levels of the ground vibronic state of the ion. The horizontal axis corresponds to the term values obtained by adding the wave-meter-calibrated visible and NIR laser frequencies to the B-$X(4,0)$ $R(0)$ transition frequency reported by Ivanov *et al.* [58]. The $GK\,^1\Sigma_g^+$ state has $3d\sigma$ character and therefore transitions to p and f Rydberg series are dominant. The strong transitions observed near the zero-quantum-defect positions of Rydberg series converging on the $N^+ = 0$ and 2 levels of HD^+ are assigned to states of the $nf0_3$ and the $nf2_N$ ($N = 1, 2, 3$) series, respectively, because of their small quantum defects and the regular nature of the progression. Several weak transitions are assigned to members of the $np0_1$ series and their positions, predicted by MQDT calculations neglecting the spin fine and hyperfine structures, are indicated by vertical green dotted lines. These transitions can only be distinguished in the spectrum of Fig. 2 near the zero-quantum-defect positions of series converging to $N^+ = 2$, where the shifts in the effective quantum defects caused by the interaction with the $np2_1$ series are the largest.

Even though the $nf0_3$ Rydberg series is nonpenetrating and displays a small average effective quantum defect of $\bar{\mu} \approx 5 \times 10^{-3}$, the binding energies of the $nf0_3$ states cannot be accurately described by Rydberg's formula

$$E_n/(hc) = -\frac{\mathcal{R}_{\mathrm{HD}}}{(n - \bar{\mu})^2} \tag{2}$$

because of rovibrational channel interactions. For most of the $nf0_3$ states, the rotational interaction with members of the $nf2_3$ series is the strongest one, leading to deviations from Eq. (2) of up to 100 MHz for $nf0_3$ states with $n > 40$.

In H_2 and D_2, nf binding energies can be calculated by MQDT with accuracies on the order of 500 kHz [26,27]. In HD, the mass asymmetry of the ionic core leads to a dipole moment which can mix Rydberg series differing in ℓ by ± 1. This effect was previously observed and quantified for the $np1_1$ series in HD [46], where good agreement with the MQDT calculations was observed, except for a 20-MHz discrepancy in the binding energy of the $56p1_1$ state. This discrepancy was attributed to a g/u-symmetry-breaking interaction with the $30d2_1$ state, which was observed in the same spectrum around 2 GHz above the $56p1_1$ state. Sprecher and Merkt [46] fitted a two-channel quantum-defect model to the experimental data, determining an effective off-diagonal quantum defect $\mu_{pd} = 2.3(3) \times 10^{-3}$.

In the case of the $nf0_3$ series, g/u mixing can occur with both the $nd1_3$ and $ng1_3$ series. Figures 3(a) and 3(b)

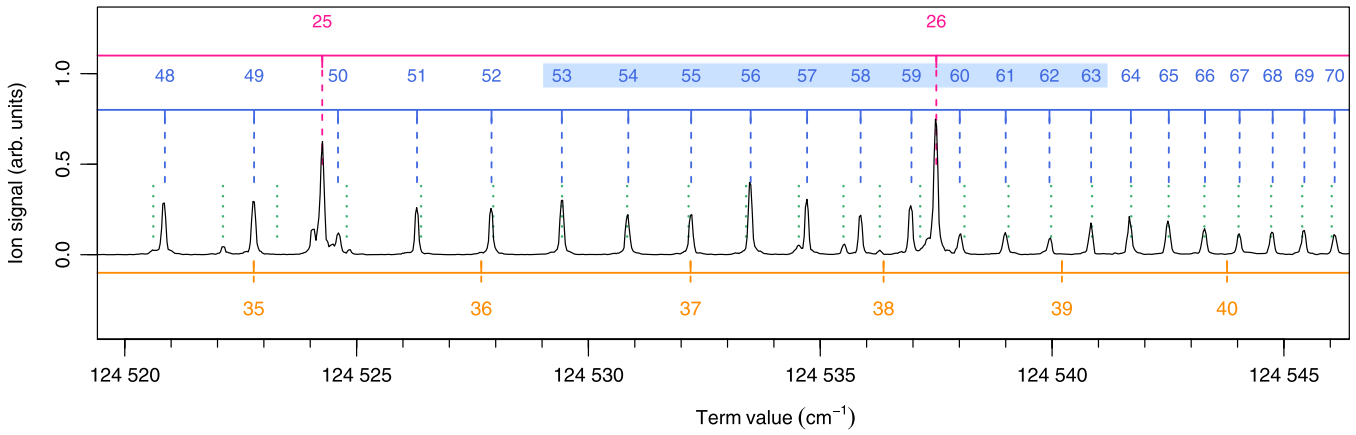

FIG. 2. Pulsed laser spectrum of the nf and np series from the $GK(0,2)$ initial state of HD below the first ionization threshold. The term value was obtained from the wave-meter calibration of the lasers together with the term value of the $B(4,1)$ state from Ref. [58]. The pink, blue, and orange axes (from top to bottom) denote the zero-quantum-defect positions of Rydberg series converging onto the $N^+ = (2, 0, 1)$ rotational states of the vibrational ground state of the ion core, respectively. The green dotted lines denote the predicted positions of the $np0_1$ series from MQDT calculations neglecting spin. The blue-shaded stripe marks all $nf0_3$ states which were used for the MQDT extrapolation (see Table III).

TABLE III. Experimental positions (in the wave-number unit of cm^{-1}) of $nf(N^+ = 0, N = 3)$ Rydberg states (ungerade symmetry) of HD relative to the $(G_1^+ = 0, G^+ = F^+ = 1)$ hyperfine component of the $65f0_3$ Rydberg state at 12 897.096 008(1)$_{stat}$(4)$_{sys}$ cm^{-1} [386 645 211.33(4)$_{stat}$(13)$_{sys}$ MHz, see Table II]. The third column gives the deviations between experiment and theoretical calculations which do not include any g/u-symmetry-mixing interactions. The calculated energies correspond to negative total parity and a total angular momentum $F = 2.5$ and were assumed to match the experimental ones at the center of gravity of $n = 57$. Calculated and experimental energies are compared in the form of a Lu-Fano plot in Fig. 4.

$nf0_3(G_1^+, G^+)$	$\tilde{\nu}_{obs}$ (cm^{-1})	$\nu_{calc-obs}$ (MHz)
$53f0_3(0, 1)$	−13.093 9529(25)	−2.50
$53f0_3(1, 0)$	−13.067 4312(37)	−2.76
$53f0_3(1, 1)$	−13.064 6548(26)	−2.80
$53f0_3(1, 2)$	−13.060 2949(23)	−2.65
$54f0_3(0, 1)$	−11.660 5947(25)	0.49
$54f0_3(1, 0)$	−11.634 0776(46)	0.37
$54f0_3(1, 1)$	−11.631 3097(20)	0.55
$54f0_3(1, 2)$	−11.626 9319(23)	0.17
$55f0_3(0, 1)$	−10.302 6088(32)	−59.19
$55f0_3(1, 0)$	−10.276 0894(41)	−59.38
$55f0_3(1, 1)$	−10.273 3316(36)	−58.90
$55f0_3(1, 2)$	−10.268 9589(23)	−59.16
$56f0_3(0, 1)$	−9.020 5239(23)	−2.26
$56f0_3(1, 0)$	−8.994 0132(31)	−2.16
$56f0_3(1, 1)$	−8.991 2354(24)	−2.30
$56f0_3(1, 2)$	−8.986 8680(22)	−2.40
$57f0_3(0, 1)$	−7.803 6526(24)	0.07
$57f0_3(1, 0)$	−7.777 1514(41)	0.43
$57f0_3(1, 1)$	−7.774 3628(19)	−0.10
$57f0_3(1, 2)$	−7.770 0020(30)	−0.07
$58f0_3(0, 1)$	−6.649 4970(26)	5.75
$58f0_3(1, 0)$	−6.622 9852(32)	5.79
$58f0_3(1, 1)$	−6.620 2180(24)	5.90
$58f0_3(1, 2)$	−6.615 8483(21)	5.67
$59f0_3(0, 1)$	−5.554 2807(37)	−5.14
$59f0_3(1, 0)$	−5.527 7633(100)	−5.27
$59f0_3(1, 1)$	−5.524 9915(28)	−5.36
$59f0_3(1, 2)$	−5.520 6292(22)	−5.43
$60f0_3(0, 1)$	−4.507 4209(22)	0.65
$60f0_3(1, 0)$	−4.480 9053(37)	0.57
$60f0_3(1, 1)$	−4.478 1309(23)	0.50
$60f0_3(1, 2)$	−4.473 7658(25)	0.41
$61f0_3(0, 1)$	−3.517 8907(19)	2.08
$61f0_3(1, 0)$	−3.491 3712(32)	1.89
$61f0_3(1, 1)$	−3.488 5959(22)	1.76
$61f0_3(1, 2)$	−3.484 2391(20)	1.92
$62f0_3(0, 1)$	−2.574 8491(20)	11.39
$62f0_3(1, 0)$	−2.548 3341(26)	11.33
$62f0_3(1, 1)$	−2.545 5724(18)	11.61
$62f0_3(1, 2)$	−2.541 2096(19)	11.55
$63f0_3(0, 1)$	−1.675 4736(26)	−1.04
$63f0_3(1, 0)$	−1.648 9630(29)	−0.94
$63f0_3(1, 1)$	−1.646 1884(23)	−1.07
$63f0_3(1, 2)$	−1.641 8281(19)	−1.05
$65f0_3(0, 1)$	+0.000 0000(0)	−9.93

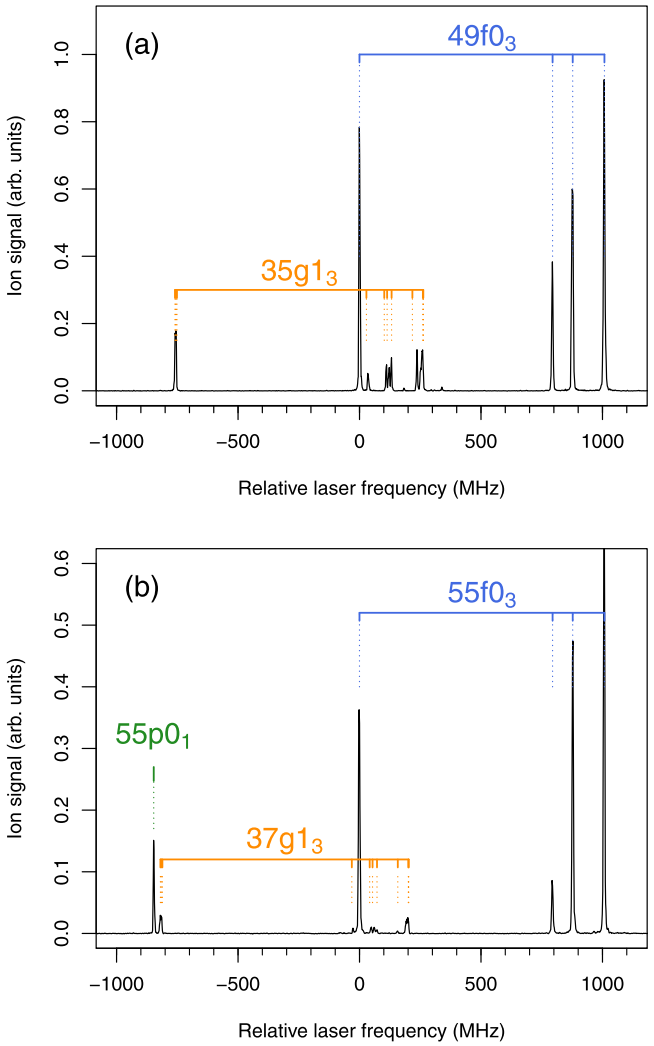

FIG. 3. High-resolution laser spectra of HD in the region of (a) the $49f0_3 \leftarrow GK(0, 2)$ transition and (b) the $55f0_3 \leftarrow GK(0, 2)$ transition, where the frequency scales were referenced to 12 877.366 and 12 886.794 cm^{-1}, respectively. Weak additional transitions to nonpenetrating Rydberg states are observed because of g/u-symmetry mixing. They are assigned to the $35g1_3$ and $37g1_3$ states, respectively, as indicated in orange color. All assignment bars correspond to the hyperfine structure of the respective rotational levels of HD^+, taken from Ref. [60].

display high-resolution laser spectra of the transitions from $GK(0,2)$ to the $49f0_3$ and $55f0_3$ states recorded with the narrow-band cw laser. The blue assignment bars indicate the hyperfine splittings of the $(v^+ = 0, N^+ = 0)$ level of HD^+, taken from Ref. [61], which agree very well with the observed hyperfine structure of the nonpenetrating $nf0_3$ states. The hyperfine structure of HD^+ has recently been calculated [23] and measured [18–20] at high accuracy, and a detailed discussion of the angular momentum coupling in Rydberg states of HD can be found in Refs. [46,62]. The main splitting of roughly 1 GHz originates from the coupling of the electron and proton spins in HD^+ ($\vec{G}_1^+ = \vec{S}^+ + \vec{I}_p$), whereas the smaller splitting of the upper $G_1^+ = 1$ component into three hyperfine

levels results from the weaker coupling to the deuteron spin ($\vec{G}^+ = \vec{G}_1^+ + \vec{I}_d$). In contrast, penetrating low-ℓ Rydberg states do not exhibit the hyperfine splitting of the HD^+ ion core because the exchange interaction between the core and Rydberg electron dominates the fine and hyperfine structure. In this case, the resulting hyperfine components have almost pure singlet or triplet character, of which only the former can be excited from the $GK\,^1\Sigma_g^+$ state. As illustration, the spectrum in Fig. 3(b) shows the transition to the $55p0_1$ ($S = 0$) state. Because $N^+ = 0$ and $S = 0$, its hyperfine structure is far too small to be resolved. MQDT calculations predict the singlet-triplet splitting to be around 11 GHz, the triplet states lying above the singlet states. Additional weak lines are observed in both panels of Fig. 3 and are attributed to transitions to nonpenetrating Rydberg states because their hyperfine structure corresponds to the one of HD^+, as explained above. These states are observed close to the zero-quantum-defect positions of Rydberg series converging on the $N^+ = 1$ level of HD^+ at effective principal quantum numbers of 34.997 and 36.997, respectively. They can therefore be assigned to the $35g1_3$ and $37g1_3$ Rydberg states. Their hyperfine splittings closely correspond to those of the $N^+ = 1$ level of HD^+, as indicated by the orange assignment bars in Fig. 3. The additional splittings in the hyperfine structure of the $N^+ = 1$ level come from the interaction between $\vec{G}^+$ and $\vec{N}^+$, which vanishes in the case of $N^+ = 0$.

In order to quantify the perturbations of the $nf0_3$ series arising from g/u-symmetry breaking, the positions of all hyperfine components of the $nf0_3$ Rydberg states with principal quantum numbers n in the range from 53 to 63 (see the light-blue-shaded stripe in Fig. 2) were measured relative to the ($G_1^+ = 0, G^+ = F^+ = 1$) hyperfine component of the $65f0_3$ Rydberg state. The laser-beam alignment remained unchanged throughout individual measurement cycles, but the back-reflected laser beam was blocked to avoid spectral congestion and to reduce the frequency range that had to be scanned. Thus, single Doppler components were measured and the Doppler-free positions were obtained by comparing with the position of the reference level, i.e., $12\,897.096\,008(1)_{\rm stat}(4)_{\rm sys}$ $\rm cm^{-1}$ [$386\,645\,211.33(4)_{\rm stat}(13)_{\rm sys}$ MHz, see Table II], which was recorded at the beginning and the end of each cycle.

The measured relative positions $\tilde{\nu}_{\rm obs}$ are given in the second column of Table III and were obtained from fits of Voigt profiles to the lines of the frequency-comb-calibrated spectra. Line profiles with full widths at half maximum in the range between 5 and 6 MHz were observed.

These positions are compared to the binding energies obtained from MQDT calculations neglecting g/u-mixing interactions, which are also referenced to the binding energy of the $65f0_3(G_1^+ = 0, G^+ = 1)$ hyperfine level. The $\ell = 3$ quantum-defect functions used in the MQDT calculations were extracted from *ab initio* Born-Oppenheimer potential-energy curves for low-n states [63,64], without adjustment to experimental data. In comparison with the quantum defects used in the previous study of D_2 [27], the energy dependence of the quantum-defect functions was improved through the inclusion of additional potential-energy curves in the extraction procedure.

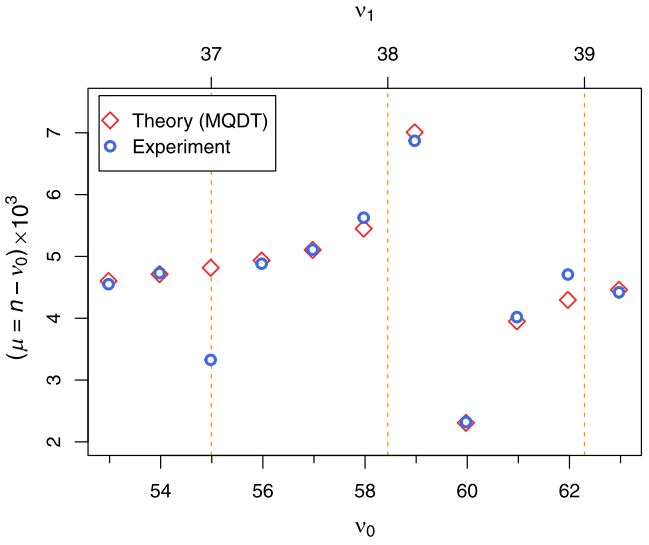

FIG. 4. Lu-Fano plot of the center-of-gravity positions of the hyperfine structure of the $nf0_3$ series in HD. The respective quantum defects are plotted as a function of the effective principal quantum number ν_{N^+} with respect to the $N^+ = 0$ threshold (bottom axis) and the $N^+ = 1$ threshold (top axis). Blue circles mark the experimental results (see Table III) and red diamonds indicate binding energies obtained from the MQDT calculations which do not include any g/u-mixing interactions.

The deviations between calculated and experimental positions are listed in the third column of Table III. They are typically large, up to 60 MHz, and vary both in magnitude and sign. These large discrepancies can be attributed to g/u-symmetry-breaking d-f and f-g interactions. Figure 4 compares the center-of-gravity positions of the hyperfine structure of the members of the $nf0_3$ series obtained from both experiment and MQDT calculations in the form of a Lu-Fano plot [65], i.e., a plot in which the spectral positions are given as their corresponding effective quantum defects $\bar{\mu}$. They are plotted against the alternative choices of effective principal quantum number ν_{N^+} with respect to the excited $N^+ = 0$ and 1 ionization thresholds, defined by Rydberg's formula $T_i = T_{N^+} - \mathcal{R}_{\rm HD}/\nu_{N^+}^2$. In the absence of channel interactions, the effective quantum defects are expected to be constant. The most prominent feature is a tangentlike behavior of the quantum defects centered between the $59f0_3$ and $60f0_3$ states. This behavior is well described by the MQDT calculations and can unambiguously be attributed to the rotational channel interaction with the $26f2_3$ state, which appears as a strong line in the laser spectrum shown in Fig. 2. The largest discrepancies between calculated and measured relative line positions are observed close to integer effective principal quantum numbers ν_1 which are marked by vertical dashed lines in Fig. 4. This behavior is expected because, at these positions, interactions with $\ell = 2, 4$ Rydberg series converging on $N^+ = 1$ are expected to have the largest effect. This, in turn, provides strong evidence that the dominant source of the discrepancies is g/u-symmetry-breaking interactions with $n\ell1_3$ Rydberg series, as manifested in the observation of transitions to the $35g1_3$ and $37g1_3$ states shown in Fig. 3.

The effect of the g/u-symmetry-breaking interactions on the hyperfine splittings of the $nf0_3$ states is much weaker than on the centers of gravity of the hyperfine structure. The deviations among each set of hyperfine components (G_1^+, G^+) are equal within ≈500 kHz, as listed in the last column of Table III. Nevertheless, these discrepancies are relevant if the level of accuracy achieved in the $GK(1,2)$-$X(0,0)$ transition frequency (380 kHz) is to be matched by the Rydberg-series extrapolation. Figures 5(a)–5(d) compare the predicted and observed hyperfine splitting for all measured states and Fig. 5(e) illustrates the angular-momentum coupling scheme. Horizontal green lines mark the hyperfine splittings of the $(v^+ = 0, N^+ = 0)$ ground state of the HD^+ ion core [60]. These splittings result from coupling of the proton spin $\vec{I}_p$, deuteron spin $\vec{I}_d$, and core electron spin $\vec{S}^+$ to form the total spin of the ion core $\vec{G}^+$. In nonpenetrating Rydberg states, the ionic hyperfine levels with $G^+ > 0$ are split into two components from coupling with the Rydberg electron spin $\vec{s}$, forming the total spin $\vec{G} = \vec{G}^+ + \vec{s}$ [see Fig. 5(e)]. Correspondingly, gray squares in Figs. 5(a)–5(d) indicate the Rydberg hyperfine levels relative to their center of gravity calculated by MQDT without considering g/u-mixing interactions. At the n values of interest, the spin-orbit interaction of the Rydberg electron is negligible and any further splitting of the levels resulting from coupling the Rydberg orbital angular momentum $\vec{F} = \vec{G} + \vec{\ell}$ is at most on the order of 10 kHz and thus not relevant for the present analysis.

The splittings into two G components are on the order of 1 MHz for the upper two hyperfine levels of the ion and can therefore not be resolved at the experimental linewidths of ≈5 MHz. However, the splittings are large enough that they need to be taken into account if the fitted line centers should be compared to the calculated positions, because different singlet characters of the components can shift the line centers by several hundred kHz. To determine the line centers, the positions calculated by MQDT, without consideration of the g/u-breaking interactions, were averaged for each G^+ component (corresponding to each observed line) and weighted with the sum of all squared coefficients of the MQDT eigenvectors having singlet $(S = 0)$ character. These positions are indicated as red diamonds in Figs. 5(a)–5(d). It should be noted that the $(G^+ = 2, G = 5/2)$ component has no singlet character, because the maximum total nuclear spin is $I = 3/2$. The measured relative line positions are shown as blue circles with error bars and show significant and systematic deviations for the upper two components. The deviations are largest for states around the positions of $n\ell 1_3$ perturbing states, which are indicated as vertical orange dotted lines. This indicates that the g/u-symmetry-breaking interactions affect the hyperfine structure of the upper two measured components of the nf Rydberg states $[(G_1^+ = 1, G^+ = 1)$ and $(G_1^+ = 1, G^+ = 2)]$ at the level of several hundred kHz whereas the other two components are not affected at the present experimental resolution. In contrast, the splitting of the lower two hyperfine levels is predicted to be below the experimental resolution. The measured line positions agree within statistical uncertainties with the hyperfine splitting of the ion [60] (green dotted lines), with the exception of $n = 57$ which is regarded as an outlier, because no perturbing state lies nearby.

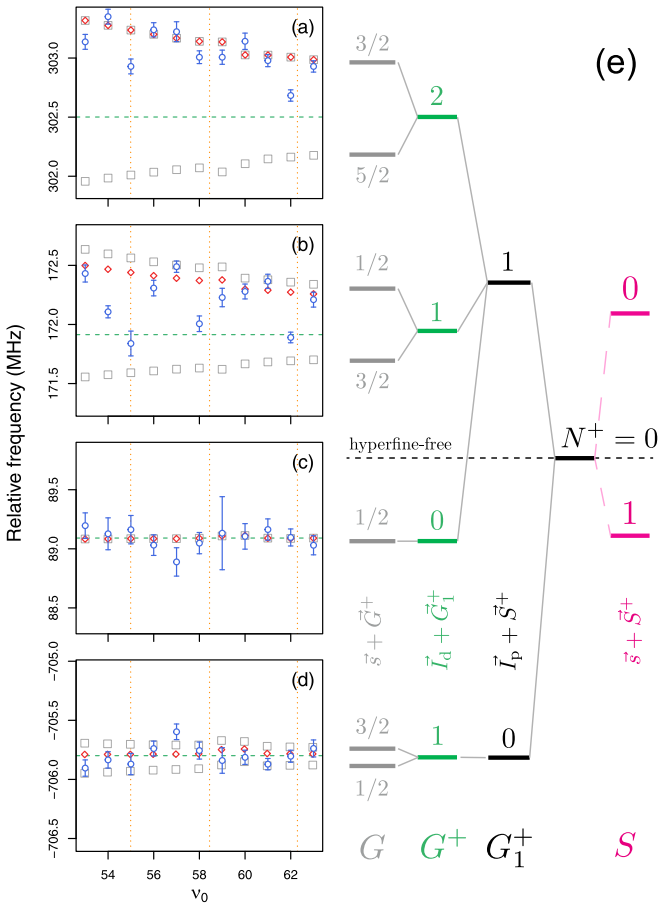

FIG. 5. (a–d) Comparison of the predicted and observed hyperfine splitting in the $nf0_3$ states of HD. The positions of the $n\ell 1_3$ perturbing states are indicated as vertical orange dotted lines. Horizontal green dashed lines mark the hyperfine splitting in the rovibrational ground state of the ion and gray squares represent the calculated level positions of the Rydberg states with respect to the center of gravity of the hyperfine structure. The red diamonds mark the expected line positions, obtained from summing the components for each value of G^+ weighted with their singlet character. Relative experimental positions are indicated in blue. For comparison, the mean of the lower two lines is set at the mean of the corresponding $G = 1/2$ and $3/2$ levels of the ion on the right-hand side of panel (d). The four displayed frequency ranges are equal. (e) The left side shows the coupling scheme for nonpenetrating Rydberg states of HD converging on the rotational ground state $N^+ = 0$ of the ion. The spin-orbit interaction of the Rydberg electron is neglected (see text for details). The right side (magenta) shows the coupling into singlet and triplet states if the nuclear spins are neglected. The spins of the proton, deuteron, core electron, and Rydberg electron are labeled $\vec{I}_p$, $\vec{I}_d$, $\vec{S}^+$, and $\vec{s}$, respectively.

Consequently, these two hyperfine components can be combined with the theoretical hyperfine splitting of HD^+, which can be assumed exact at the present experimental uncertainty, to obtain hyperfine-free positions of the $nf0_3$ Rydberg series that are independent of the effects of g/u-symmetry-breaking interactions on the hyperfine structure. In Figs. 5(a)–5(d), the mean of the lower two observed line positions was referenced to the mean of corresponding ionic hyperfine levels $[G = 1/2$ and $3/2$ levels on the left-hand side of Fig. 5(d)].

IV. MQDT TREATMENT OF g/u-SYMMETRY-BREAKING INTERACTIONS

The observed effective quantum defects shown in Fig. 4 demonstrate that g/u-symmetry breaking can cause significant shifts of the $nf0_3$ series not only when the perturbing $ng1_3$ levels are directly observed, as in Fig. 3, but also in cases where the perturbing states remain unobserved in the spectra. In order to accurately describe the observed nf positions, it is therefore necessary to take into account g/u-symmetry-breaking interactions of the $nf0_3$ series with both the $nd1_3$ series (d-f interaction) and the $ng1_3$ series (f-g interaction).

Such interactions are mediated by the dipole moment of the HD^+ ion core. To model its influence on the nf states, off-diagonal quantum-defect elements η_{df} and η_{fg} were introduced into the MQDT calculations, a treatment following previous work describing the p-f interaction arising from the quadrupole moment of the ion core [35]. The inclusion of effects of a core dipole moment into the molecular MQDT theory has been discussed in Sec. 4.2.2 of Ref. [33]. For simplicity, any dependence of η_{df} and η_{fg} on energy, spin, internuclear distance, and projection Λ of the total orbital angular momentum on the internuclear axis was neglected. η_{df} and η_{fg} were refined in a least-squares-fit procedure to minimize the scatter in the binding energies of the $GK(0,2)$ level, which were obtained for each nf Rydberg level as the sum of the observed transition frequency and the binding energy calculated by MQDT. The eigenchannel quantum-defect functions of the perturbing series used in the calculations were $\ell = 2$ quantum-defect functions previously derived [66] using a procedure developed by Ross and Jungen [67], and spin-independent $\ell = 4$ quantum-defect functions obtained from a core-polarization model [34,68].

In order to reduce the computational complexity of the fit, hyperfine interactions were neglected and the MQDT calculations were performed with the two sets of singlet ($S = 0$) and triplet ($S = 1$) quantum defects. The calculated hyperfine-free line positions were obtained from a weighted fit of the singlet and triplet positions. For comparison, the experimental hyperfine-free line positions were determined from the lowest two measured components [$(G_1^+ = 0, G^+ = 1)$ and $(G_1^+ = 1, G^+ = 0)$] for each $nf0_3$ state, as discussed in Sec. III.

The two members of the $ng1_3$ series which could be directly observed in the spectrum (see Fig. 3) give additional information for the adjustment of the off-diagonal quantum defects, in particular for η_{fg}. As above, we obtain information about the hyperfine-free position of the $ng1_3$ states from their lowest hyperfine components ($G_1^+ = 0, G^+ = 1$). Because of the presence of rotational excitation of the core, these components exhibit an additional splitting into hyperfine levels ($F^+ = 0, 1, 2$). This splitting is of the order of several MHz and was taken into account in the line-shape model used to fit the spectra. No Doppler-free positions of the $ng1_3$ states were determined in this investigation, but the positions of the lowest hyperfine components of the $35g1_3$ and $37g1_3$ states could be determined relative to the ($G_1^+ = 0, G^+ = 1$) components of the $49f0_3$ and $55f0_3$ states, respectively, from frequency-comb-calibrated spectra. These two hyperfine-free f-g distances were included in the refinement of the off-diagonal quantum defects.

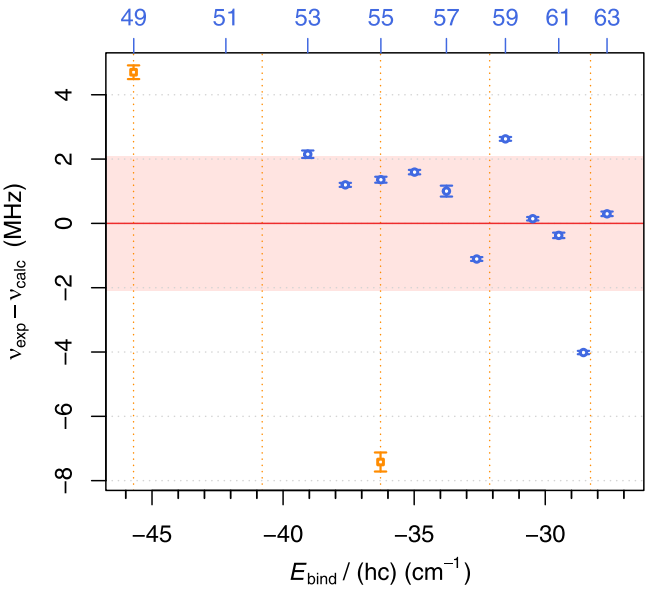

FIG. 6. Residuals of the binding energies of the $GK(0,2)$ state (blue dots), determined from the measured positions of the $nf0_3$ states together with their binding energies predicted from MQDT. The standard deviation of the fitted binding energy is indicated by the red shaded area. Orange squares indicate the differences between measured f-g distances as seen in Fig. 3 and the calculation (see text for details).

Figure 6 displays the residuals resulting from this optimization, with the residuals for the Doppler-free positions of the $nf0_3$ states shown in blue and the residuals for the f-g distances shown in orange. The positions of the $n\ell 1_3$ states are indicated by vertical dotted orange lines. The mean value of the binding energy of the $GK(0,2)$ level was determined to be 12 923.091 91(7) cm^{-1} from the resulting Doppler-free positions of the $nf0_3$ states and the red shaded area displays the associated uncertainty (1σ) of 2.1 MHz. The off-diagonal quantum defects were fitted to $\eta_{df} = 2.7(6) \times 10^{-3}$ and $\eta_{fg} = 2.81(3) \times 10^{-3}$. These values are comparable to the value of the p-d off-diagonal quantum defect $\eta_{pd} = 2.3(3) \times 10^{-3}$ obtained in Ref. [46]. The residuals obtained for the $nf0_3$ series (blue dots in Fig. 6) are much improved in comparison to those listed in Table III. Nevertheless, the remaining scatter of several MHz still suggests an incomplete description of the g/u-symmetry-breaking interactions. The magnitude of these deviations justifies the hyperfine-free approach followed in the present investigation to model the Rydberg states. Further investigations might focus on the dependence of the off-diagonal quantum defects on the spin and the projection Λ of the orbital angular momentum and take into account the observed hyperfine structure of the Rydberg states.

V. CONCLUSIONS AND OUTLOOK

The first three rows of Table IV give the intervals determined in the present investigation with their uncertainties. Combining these intervals yields a new value of 124 568.484 66(7) cm^{-1} for the ionization energy of HD. With the latest values of the ionization energies E_I(H), E_I(D), and $E_I(HD^+)$ of the H atom [24], the D atom [69,70], and HD^+

TABLE IV. Ionization and dissociation energies of HD from the present measurements, and comparison with previous results and with theory.

	Energy-level interval	Value (cm^{-1})	Uncertainty (MHz)	Ref.
(1)	$GK(1,2) \leftarrow X(0,0)$	111 928.508 677(13)	0.38	This paper
(2)	$GK(1,2) \leftarrow GK(0,2)$	283.115 9262(15)	0.05	This paper
(3)	$X^+(0,0) \leftarrow GK(0,2)$	12 923.091 91(7)	2.1	This paper
(4)=(1)−(2)+(3)	E_I(HD)	124 568.484 66(7)	2.1	This paper
(5)	$E_I(HD^+)$	131 224.684 1650(6)	0.018	[22]
(6)	E_I(H)	109 678.771 74307(10)	0.003	[24]
(7)	E_I(D)	109 708.614 552 94(17)	0.005	[69,70]
(8)=(4)+(5)−(6)−(7)	D_0(HD)	36 405.782 53(7)	2.1	This paper
(9)	D_0(HD)	36 405.782 477(26)	0.8	Theory [4]
(8)−(9)	Obs.-calc. D_0(HD)	0.000 05(7)		

[22], respectively, a dissociation energy for HD of $D_0(\mathrm{HD}) = 36\,405.782\,53(7)\,\mathrm{cm}^{-1}$ [$= 1\,091\,417\,903.0(2.1)\,\mathrm{MHz}$] is obtained. The last three rows of Table IV compare this new result with the latest theoretical value.

The 3.2σ discrepancy between experiment and theory pointed out by Puchalski *et al.* in the case of HD [4] is thus resolved by the present measurement and there is now agreement between theory and experiment at the level of 1σ.

The present values of the ionization and dissociation energies of HD are more precise than the 2010 result of Sprecher *et al.* [38] by a factor of about 5. The present determination of the ionization energy of HD relies on intervals involving the $GK\ ^1\Sigma_g^+$ state and nf Rydberg series whereas the 2010 determination [38] relied on the $EF\ ^1\Sigma_g^+$ state and np Rydberg series. It is therefore not possible to identify the reasons for the discrepancy between the two experimental results on an interval-per-interval basis.

The increased precision of the present determination results from a series of improvements in the experimental approach and the Rydberg series extrapolation by MQDT, which were already mentioned when the results on H_2 [25] and D_2 [27] were reported. The high precision and accuracy of the $GK(1,2) \leftarrow X(0,0)$ interval were made possible by the compensation of chirps in the pulsed amplification of the Ti:Sa single-mode radiation, as detailed in Ref. [48] and by the replacement of the calibration procedure based on reference lines of I_2 in 2010 with a procedure relying on atomic clocks and frequency combs both in Amsterdam and Zurich, as explained in Refs. [12,25–27]. In Zurich, the excitation of np Rydberg series from the EF intermediate state with pulsed UV radiation was replaced by the excitation of nf Rydberg series from the GK intermediate state with single-mode cw NIR laser radiation. The advantages of this excitation are threefold: Firstly, the NIR cw excitation enabled the reduction of the linewidths by a factor of more than 10. Secondly, the generation of high ion concentrations, which is inevitable when preparing the EF intermediate state by nonresonant two-photon excitation, could be avoided, limiting line shifts and inhomogeneous broadenings through the Stark effect induced by the fields of the ions. Thirdly, the f Rydberg series accessed from the GK state are nonpenetrating series and thus less perturbed than the p series, as already explained in Ref. [26], resulting in a more precise extrapolation of the series. Finally, significant progress was also made in the treatment, by MQDT, of g/u interactions, as detailed in Sec. IV. These were not considered in the 2010 determination [38].

The new value for D_0(HD) is compared in Fig. 7(a) with the previous experimental value obtained in 2010 [38] and with the theoretical values from 2010 to 2019 [4,43,71]. Experimental and theoretical values are plotted in blue and red, respectively. The values are ordered according to their publication date with the newest results at the top. The new value of the dissociation energy of HD determined here lies 33 MHz below the value determined in 2010 via the $EF(0,0)$ intermediate state [38]. Two effects may explain this discrepancy. First, the 2010 experiments were carried out in a noncompensated field of 28(7) mV/cm and the resulting Stark shift was subtracted from the measured position of the

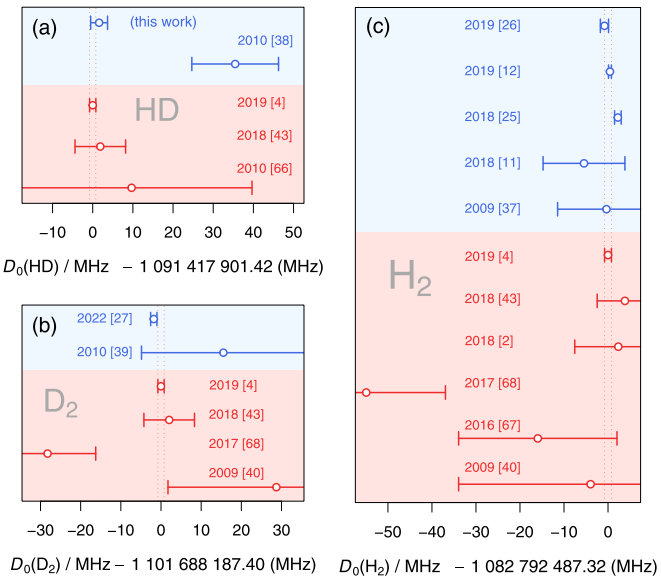

FIG. 7. Comparison of the progress made in the last 13 years in the determination of the dissociation energies of (a) HD, (b) D_2, and (c) H_2 in experimental (blue) [11,12,25–27,37–39] and theoretical (red) [2,4,40,43,71–73] work. The horizontal axes are referenced to the most recent theoretical values of Puchalski *et al.* [4] and the corresponding 1σ intervals of ± 0.8 MHz are indicated by vertical dotted lines.

$64p0_1$ Rydberg state. Additional positive Stark shifts from ions in the measurement volume are enhanced compared to a situation where the stray fields are compensated, as in the 2009–2010 experiments on H_2 and D_2 [37,39], and our systematic-uncertainty analysis for the determination of the HD ionization energy did not take this effect into account. In addition, the g/u interaction, which was recognized later to be significant in HD [46], was neglected in the 2010 analysis. We therefore estimate that the systematic uncertainty of the 2010 determination of the HD dissociation and ionization energies was underestimated by about 30 MHz.

For comparison, Figs. 7(b) and 7(c) depict the results for D_2 and for H_2, respectively. The frequency axes of all three panels are referenced to the latest theoretical values for the dissociation energies published by Puchalski *et al.* in 2019 [3,4]. In all three panels of Fig. 7, the most recent experimental values were determined by two-photon spectroscopy of the GK state and Rydberg-series extrapolation using nf states. The current agreement in the theoretical and experimental values of the dissociation energy of H_2, HD, and D_2 at the $\Delta\nu/\nu = 10^{-9}$ level is remarkable and confirms molecular hydrogen as an attractive system for metrology.

The main limitation in the precision of the value of D_0(HD) lies in the extrapolation of the ionization energy by MQDT. In the future, two strategies can be followed to improve the accuracy of the extrapolation. The first consists in improving the description of the nf Rydberg states of HD by MQDT, primarily the description of their interactions with nd and ng Rydberg series. The second approach consists in determining the zero-quantum-defect positions from high-resolution Stark spectra of the Rydberg-Stark manifolds [74], for which an accuracy of better than 100 kHz is anticipated.

ACKNOWLEDGMENTS

The authors thank M. Silkowski and K. Pachucki (Warsaw) for making available further potential-energy curves for excited states of hydrogen prior to publication. K.S.E.E., F.M., and W.U. acknowledge financial support from European Research Council advanced grants under the European Union's Horizon 2020 research and innovation program (Grants No. 695677, No. 743121, and No. 670168). H.L.B., K.S.E.E., and W.U. acknowledge NWO for a program grant on "The mysterious size of the proton." F.M. acknowledges financial support from the Swiss National Science Foundation (Project No. 200020B-200478 and Sinergia Grant No. CRSII5-183579). M.B. acknowledges NWO for a VENI grant (Grant No. VI.Veni.202.140).

[1] B. Simmen, E. Mátyus, and M. Reiher, Mol. Phys. **111**, 2086 (2013).
[2] L. M. Wang and Z.-C. Yan, Phys. Rev. A **97**, 060501(R) (2018).
[3] M. Puchalski, J. Komasa, P. Czachorowski, and K. Pachucki, Phys. Rev. Lett. **122**, 103003 (2019).
[4] M. Puchalski, J. Komasa, A. Spyszkiewicz, and K. Pachucki, Phys. Rev. A **100**, 020503(R) (2019).
[5] W. Ubachs, J. C. J. Koelemeij, K. S. E. Eikema, and E. J. Salumbides, J. Mol. Spectrosc. **320**, 1 (2016).
[6] S. Kassi, A. Campargue, K. Pachucki, and J. Komasa, J. Chem. Phys. **136**, 184309 (2012).
[7] L.-G. Tao, A.-W. Liu, K. Pachucki, J. Komasa, Y. R. Sun, J. Wang, and S.-M. Hu, Phys. Rev. Lett. **120**, 153001 (2018).
[8] F. M. J. Cozijn, P. Dupré, E. J. Salumbides, K. S. E. Eikema, and W. Ubachs, Phys. Rev. Lett. **120**, 153002 (2018).
[9] E. Fasci, A. Castrillo, H. Dinesan, S. Gravina, L. Moretti, and L. Gianfrani, Phys. Rev. A **98**, 022516 (2018).
[10] P. Wcisło, F. Thibault, M. Zaborowski, S. Wójtewicz, A. Cygan, G. Kowzan, P. Masłowski, J. Komasa, M. Puchalski, K. Pachucki *et al.*, J. Quant. Spectrosc. Radiat. Transfer **213**, 41 (2018).
[11] R. K. Altmann, L. S. Dreissen, E. J. Salumbides, W. Ubachs, and K. S. E. Eikema, Phys. Rev. Lett. **120**, 043204 (2018).
[12] N. Hölsch, M. Beyer, E. J. Salumbides, K. S. E. Eikema, W. Ubachs, Ch. Jungen, and F. Merkt, Phys. Rev. Lett. **122**, 103002 (2019).
[13] A. Fast and S. A. Meek, Phys. Rev. Lett. **125**, 023001 (2020).
[14] A. Castrillo, E. Fasci, and L. Gianfrani, Phys. Rev. A **103**, 022828 (2021).
[15] M. Lamperti, L. Rutkowski, D. Ronchetti, D. Gatti, R. Gotti, G. Cerullo, F. Thibault, H. Jozwiak, S. Wojtewicz, P. Maslowski, P. Wcislo, D. Polli, and M. Marangoni, Comm. Phys. **6**, 67 (2023).
[16] A. Grinin, A. Matveev, D. C. Yost, L. Maisenbacher, V. Wirthl, R. Pohl, T. W. Hänsch, and T. Udem, Science **370**, 1061 (2020).
[17] N. Bezginov, T. Valdez, M. Horbatsch, A. Marsman, A. C. Vutha, and E. A. Hessels, Science **365**, 1007 (2019).
[18] S. Alighanbari, G. S. Giri, F. L. Constantin, V. I. Korobov, and S. Schiller, Nature (London) **581**, 152 (2020).
[19] S. Patra, M. Germann, J.-P. Karr, M. Haidar, L. Hilico, V. I. Korobov, F. M. J. Cozijn, K. S. E. Eikema, W. Ubachs, and J. C. J. Koelemeij, Science **369**, 1238 (2020).
[20] I. V. Kortunov, S. Alighanbari, M. G. Hansen, G. S. Giri, V. I. Korobov, and S. Schiller, Nat. Phys. **17**, 569 (2021).
[21] S. G. Karshenboim, Phys. Rep. **422**, 1 (2005).
[22] V. I. Korobov, L. Hilico, and J.-Ph. Karr, Phys. Rev. Lett. **118**, 233001 (2017).
[23] D. T. Aznabayev, A. K. Bekbaev, and V. I. Korobov, Phys. Rev. A **99**, 012501 (2019).
[24] E. Tiesinga, P. J. Mohr, D. B. Newell, and B. N. Taylor, Rev. Mod. Phys. **93**, 025010 (2021).
[25] C.-F. Cheng, J. Hussels, M. Niu, H. L. Bethlem, K. S. E. Eikema, E. J. Salumbides, W. Ubachs, M. Beyer, N. Hölsch, J. A. Agner, F. Merkt, L.-G. Tao, S.-M. Hu, and Ch. Jungen, Phys. Rev. Lett. **121**, 013001 (2018).
[26] M. Beyer, N. Hölsch, J. Hussels, C.-F. Cheng, E. J. Salumbides, K. S. E. Eikema, W. Ubachs, Ch. Jungen, and F. Merkt, Phys. Rev. Lett. **123**, 163002 (2019).
[27] J. Hussels, N. Hölsch, C.-F. Cheng, E. J. Salumbides, H. L. Bethlem, K. S. E. Eikema, Ch. Jungen, M. Beyer, F. Merkt, and W. Ubachs, Phys. Rev. A **105**, 022820 (2022).
[28] G. Herzberg, Proc. R. Soc. A **262**, 291 (1961).

[29] A. Balakrishnan, V. Smith, and B. P. Stoicheff, Phys. Rev. A **49**, 2460 (1994).

[30] Y. P. Zhang, C. H. Cheng, J. T. Kim, J. Stanojevic, and E. E. Eyler, Phys. Rev. Lett. **92**, 203003 (2004).

[31] G. Herzberg and Ch. Jungen, J. Mol. Spectrosc. **41**, 425 (1972).

[32] D. Sprecher, Ch. Jungen, W. Ubachs, and F. Merkt, Faraday Discuss. **150**, 51 (2011).

[33] Ch. Jungen, in *Handbook of High-Resolution Spectroscopy*, edited by M. Quack and F. Merkt (Wiley, New York, 2011), Vol. 1, pp. 471–510.

[34] Ch. Jungen, I. Dabrowski, G. Herzberg, and D. J. W. Kendall, J. Chem. Phys. **91**, 3926 (1989).

[35] A. Osterwalder, A. Wüest, F. Merkt, and Ch. Jungen, J. Chem. Phys. **121**, 11810 (2004).

[36] D. Sprecher, J. Liu, T. Krähenmann, M. Schäfer, and F. Merkt, J. Chem. Phys. **140**, 064304 (2014).

[37] J. Liu, E. J. Salumbides, U. Hollenstein, J. C. J. Koelemeij, K. S. E. Eikema, W. Ubachs, and F. Merkt, J. Chem. Phys. **130**, 174306 (2009).

[38] D. Sprecher, J. Liu, Ch. Jungen, W. Ubachs, and F. Merkt, J. Chem. Phys. **133**, 111102 (2010).

[39] J. Liu, D. Sprecher, Ch. Jungen, W. Ubachs, and F. Merkt, J. Chem. Phys. **132**, 154301 (2010).

[40] K. Piszczatowski, G. Łach, M. Przybytek, J. Komasa, K. Pachucki, and B. Jeziorski, J. Chem. Theory Comput. **5**, 3039 (2009).

[41] J. Komasa, K. Piszczatowski, G. Łach, M. Przybytek, B. Jeziorski, and K. Pachucki, J. Chem. Theory Comput. **7**, 3105 (2011).

[42] C. Roth, A. Martínez de Velasco, E. L. Gründeman, M. Collombon, M. Beyer, V. Barbé, and K. S. E. Eikema, Mol. Phys. e2211405 (2023).

[43] M. Puchalski, A. Spyszkiewicz, J. Komasa, and K. Pachucki, Phys. Rev. Lett. **121**, 073001 (2018).

[44] A. Carrington and R. A. Kennedy, in *Ions and Light*, Gas Phase Ion Chemistry Vol. 3, edited by M. T. Bowers (Academic, New York, 1984), pp. 393–442.

[45] A. Carrington, I. R. McNab, and Ch. A. Montgomerie, J. Phys. B **22**, 3551 (1989).

[46] D. Sprecher and F. Merkt, J. Chem. Phys. **140**, 124313 (2014).

[47] P. Allmendinger, J. Deiglmayr, O. Schullian, K. Höveler, J. A. Agner, H. Schmutz, and F. Merkt, Chem. Phys. Chem. **17**, 3596 (2016).

[48] J. Hussels, C. Cheng, E. Salumbides, and W. Ubachs, Opt. Lett. **45**, 5909 (2020).

[49] S. Hannemann, E.-J. Van Duijn, and W. Ubachs, Rev. Sci. Instr. **78**, 103102 (2007).

[50] J. Hussels, Improved determination of the dissociation energy of H_2, HD and D_2, Ph.D. thesis, Vrije Universiteit Amsterdam, 2021, https://research.vu.nl/en/publications/improved-determination-of-the-dissociation-energy-of-h2-hd-and-d2.

[51] R. F. Code and N. F. Ramsey, Phys. Rev. A **4**, 1945 (1971).

[52] M. Puchalski, J. Komasa, and K. Pachucki, Phys. Rev. Lett. **120**, 083001 (2018).

[53] H. Jóźwiak, H. Cybulski, and P. Wcisło, J. Quant. Spectrosc. Radiat. Transfer **253**, 107171 (2020).

[54] H. Jóźwiak, H. Cybulski, A. Grabowski, and P. Wcisło, Phys. Rev. A **104**, 012808 (2021).

[55] S. Kassi, C. Lauzin, J. Chaillot, and A. Campargue, Phys. Chem. Chem. Phys. **24**, 23164 (2022).

[56] H. Jóźwiak and P. Wcisło, Phys. Rev. A **107**, 012802 (2023).

[57] N. Hölsch, M. Beyer, and F. Merkt, Phys. Chem. Chem. Phys. **20**, 26837 (2018).

[58] T. I. Ivanov, G. D. Dickenson, M. Roudjane, N. de Oliveira, D. Joyeux, L. Nahon, W.-Ü. L. Tchang-Brillet, and W. Ubachs, Mol. Phys. **108**, 771 (2010).

[59] M. Beyer, N. Hölsch, J. A. Agner, J. Deiglmayr, H. Schmutz, and F. Merkt, Phys. Rev. A **97**, 012501 (2018).

[60] V. I. Korobov, Phys. Rev. A **77**, 022509 (2008).

[61] D. Bakalov, V. I. Korobov, and S. Schiller, Phys. Rev. Lett. **97**, 243001 (2006).

[62] D. Sprecher, Ch. Jungen, and F. Merkt, J. Chem. Phys. **140**, 104303 (2014).

[63] M. Siłkowski, M. Zientkiewicz, and K. Pachucki, Adv. Quantum Chem. **83**, 255 (2021).

[64] M. Siłkowski and K. Pachucki (private communication).

[65] K. T. Lu and U. Fano, Phys. Rev. A **2**, 81 (1970).

[66] D. Sprecher, Rovibronic and hyperfine interactions in Rydberg states of molecular hydrogen, Ph.D. thesis, ETH Zurich, 2013, https://www.research-collection.ethz.ch/handle/20.500.11850/74157.

[67] S. C. Ross and Ch. Jungen, Phys. Rev. A **49**, 4353 (1994).

[68] Ch. Jungen, I. Dabrowski, G. Herzberg, and M. Vervloet, J. Chem. Phys. **93**, 2289 (1990).

[69] V. A. Yerokhin, K. Pachucki, and V. Patkóš, Ann. Phys. (NY) **531**, 1800324 (2019).

[70] V. A. Yerokhin (private communication).

[71] K. Pachucki and J. Komasa, Phys. Chem. Chem. Phys. **12**, 9188 (2010).

[72] M. Puchalski, J. Komasa, P. Czachorowski, and K. Pachucki, Phys. Rev. Lett. **117**, 263002 (2016).

[73] M. Puchalski, J. Komasa, and K. Pachucki, Phys. Rev. A **95**, 052506 (2017).

[74] N. Hölsch, I. Doran, M. Beyer, and F. Merkt, J. Mol. Spectrosc. **387**, 111648 (2022).